Frequency–Time Domain Analysis Based on Electrochemical Noise of Dual-Phase (DP) and Ferrite–Bainite (FB) Steels in Chloride Solutions for Automotive Applications

Facundo Almeraya-Calderón [1], Marvin Montoya-Rangel [2], Demetrio Nieves-Mendoza [3,*],
Jesús Manuel Jáquez-Muñoz [4], Miguel Angel Baltazar-Zamora [3], Laura Landa-Ruiz [3,*], Maria Lara-Banda [1],
Erick Maldonado-Bandala [3], Francisco Estupiñan-Lopez [1,*] and Citlalli Gaona-Tiburcio [1]

[1] Universidad Autonoma de Nuevo Leon, FIME, Centro de Investigación e Innovación en Ingeniería
Aeronáutica (CIIIA), s/n, Ciudad Universitaria, San Nicolás de los Garza 66455, Nuevo León, Mexico;
facundo.almerayacld@uanl.edu.mx (F.A.-C.); maria.laraba@uanl.edu.mx (M.L.-B.);
citlalli.gaonatbr@uanl.edu.mx (C.G.-T.)

[2] Unidad de Investigación y Tecnologias Aplicadas, Facultad de Química, Universidad Nacional Autónoma de
México, Apodaca 66629, Nuevo León, Mexico; marmontoya@utp.edu.co

[3] Facultad de Ingeniería Civil, Universidad Veracruzana, Xalapa 91000, Veracruz, Mexico;
mbaltazar@uv.mx (M.A.B.-Z.); erimaldonado@uv.mx (E.M.-B.)

[4] Instituto Tecnológico de Ciudad Juarez, Av. Tecnológico, 1340, Ciudad Juárez 32500, Chihuahua, Mexico;
jesus.jaquezmn@uanl.edu.mx

[*] Correspondence: dnieves@uv.mx (D.N.-M.); lalanda@uv.mx (L.L.-R.);
francisco.estupinanlp@uanl.edu.mx (F.E.-L.)

Abstract: The automotive industry uses high-strength (HS), low-alloy (HSLA) steels and advanced high-strength steels (AHSSs) to manufacture front and rear rails and safety posts, as well as the car body, suspension, and chassis components of cars. These steels can be exposed to corrosive environments, such as in countries where de-icing salts are used. This research aims to characterize the corrosion behavior of AHSSs based on electrochemical noise (EN) [dual-phase (DP) and ferrite–bainite (FB)]. At room temperature, the steels were immersed in NaCl, $CaCl_2$, and $MgCl_2$ solutions and were studied by frequency–time domain analysis using wavelet decomposition, Hilbert–Huang analysis, and recurrence plots (RPs) related to the corrosion process and noise impedance (Z_n). Optical microscopy (OM) was used to observe the microstructure of the tested samples. The results generally indicated that the main corrosion process is related to uniform corrosion. The corrosion behavior of AHSSs exposed to a NaCl solution could be related to the morphology of the phase constituents that are exposed to solutions with chlorides. The Zn results showed that DP780 presented a higher corrosion resistance with 918 $\Omega\cdot cm^2$; meanwhile, FB780 presented 409 $\Omega\cdot cm^2$ when exposed to NaCl. Also, the corrosion mechanism of materials begins with a localized corrosion process spreading to all the surfaces, generating a uniform corrosion process after some exposition time.

Keywords: corrosion; AHSSs; electrochemical noise; wavelets; Hilbert–Huang transform (HHT); recurrence plots (RPs)

1. Introduction

The use of advanced high-strength steels (AHSSs) continues to grow in the automotive sector, especially for body structures, suspension, and chassis components. This is the result of multiple characteristics, such as high formability that can be used to achieve external designs, lightness, sufficient rigidity for vehicle handling, high mechanical strength, the possibilities of production in large quantities, and the possibility of achieving all of this under strong economic limitations [1,2].

Advanced high-strength steels (AHSSs) are multi-phase metallic alloys that provide a higher balance of strength and ductility than conventional mild steels and high-strength,

low-alloy (HSLA) steels [1]. Advanced steels have been used for decades in the automotive sector; some types of steel (see Figure 1) include complex-phase (CP), transformation-induced plasticity (TRIP), hot-formed (HF), ferrite–bainite (FB), and dual-phase (DP) steels, among others [2,3].
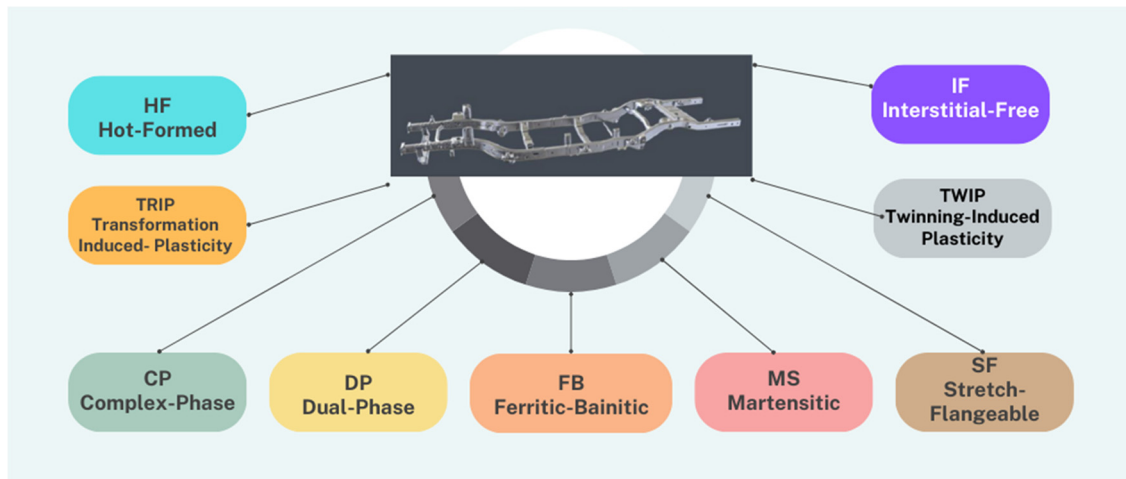

Figure 1. Classification of advanced high-strength steels (AHSSs).

The Auto/Steel Association published a document called *Advanced Applications of High Strength Steel: Design Guidelines and Stamping Process*, and in this edition, 12 detailed cases of using these steels were addressed [4]. Most of the steel parts in this document were focused on DP steel. Details are given on the component geometry, part design, secondary metallurgical processes such as forming and stamping, and indicators of mechanical properties.

Dual-phase steels have a bainite or martensite microstructure in a ferrite matrix. The microstructure of DP steels can be improved by an intercritical heat treatment consisting of two steps: first, intercritical annealing is carried out, and second, rapid cooling is performed to promote the transformation of intercritical austenite into a hard phase (martensite) [5]. To increase the hardness of DP steel (228 to 317 HV), it is necessary to perform a tempering heat treatment between 740 and 820 °C and thus obtain a higher percentage of martensite phase [6].

FB steels have a bainite microstructure in a ferrite matrix, which is obtained by austenitizing FB steel at a temperature of 1100 °C for 20–60 min, followed by air-cooling and immersion in a salt bath at temperatures of 500–800 °C for a time of 1 h, and finishing the process in a type of rapid quenching called water quenching [7–9]. It has been reported that the phase content present in AHSSs influences their mechanical properties; the minimum elongation of ferritic–bainitic steels is approximately 22%, while for dual-phase steels, it is only 8% [10]. The mechanical strength of FB steels/AHSSs is obtained from the grain size refinement, the creation of precipitates, and the high dislocation density present in the bainite phase [11]. Therefore, DP steels will enable lighter automotive production; however, using a thinner gauge strip means that corrosion resistance becomes paramount [12].

In various investigations, it has been reported that the heat treatment of AHSSs increases their corrosion resistance when there is an increase in the austenitization temperature, and it will also depend on whether the heat treatment involves annealing or quenching, due to the formation of a martensitic phase in a ferrite matrix when using DP steels. Abedini et al. [13] mentioned that an increase does not improve the corrosion resistance of DP steels in the martensitic phase. On the other hand, biphase steels have a higher corrosion resistance than conventional steels due to the formation of galvanic pairs between martensite and ferrite or pearlite and ferrite, the latter being more susceptible. In FB steels, corrosion resistance is lower due to the creation of galvanic pairs, compared to DP steels. However, this resistance can be increased by grain size refinement in FB steel, which also improves its resistance to pitting and intergranular corrosion. However, the information in the literature is limited when addressing the corrosion mechanism and

kinetics of AHSSs [14,15]. Some chemical elements, such as magnesium, do not help to improve corrosion resistance, whereas silicon does [15].

Figure 2 shows the banana diagrams for steel. The AHSS presents an elongation lower than 30%, supporting tensile stress until 1600 MPa, depending on the type of AHSS, compared with conventional steels that only support values lower than 700 MPa and present elongation until 65% [16].
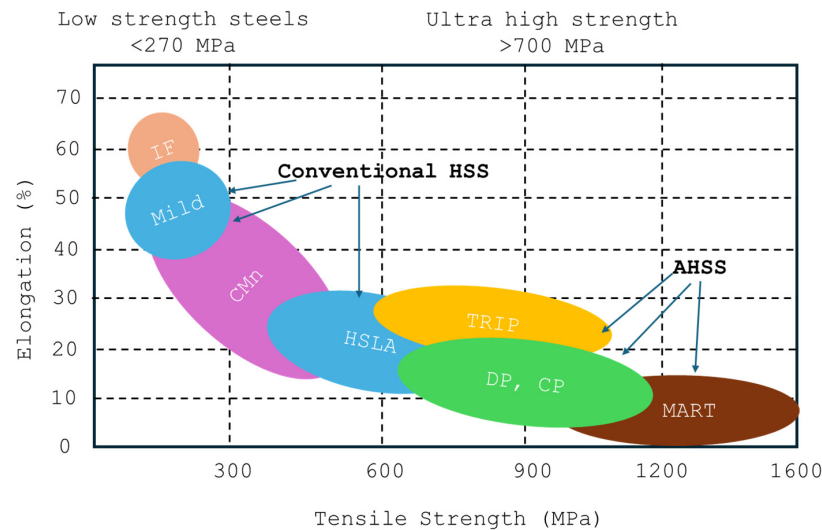

Figure 2. Elongation (%) vs. tensile strength (MPa) banana diagrams for the different types of steels.

Corrosion studies using conventional electrochemical techniques allow for determining the mechanism and kinetics of corrosion of metallic materials immersed in corrosive environments. Direct or alternating current electrochemical techniques usually disturb the system under study, such as potentiodynamic polarization (PP), linear polarization resistance (LPR), galvanodynamic polarization (GP), and electrochemical impedance spectroscopy (EIS). The alteration can be caused by external signals or experimentation conditions [17]. On the other hand, there is electrochemical noise (EN), whose measurements do not disturb the system under study, and current and voltage signal fluctuations occur on the electrode surface due to corrosion processes and not by an external signal, as in other corrosion techniques. Oxidation and reduction reactions are associated with transients as a response to stochastic processes (the breakdown and re-passivation of the passive layer) and deterministic processes (the nucleation and growth of pits) [18–20]

EN measurements allow for the obtaining of data that several methods can analyze. In the time domain (statistical analysis such as electrochemical noise resistance (R_n), Kurtosis, Skewness, Localization Index (L.I.)); in the frequency domain (spectral densities), and in the time–frequency domain (wavelet decomposition, Hilbert–Huang analysis, and recurrence plots (RP)) [21–25].

Several studies have indicated that the corrosion kinetics obtained from potentiodynamic tests in 3.5 wt. % NaCl solution at room temperature have shown that the corrosion rate decreases when there are ferrite–martensite phases (DP steels) compared to when there are ferrite–pearlite phases (carbon steel) due to the galvanic couple that is formed [13,26]. Montoyaand Nagiub found similar behavior for different dual-phase steels in an electrolyte with chloride ions [2,27]. Ikpeseni et al. indicated that dual-phase steel exhibits corrosion potentials between carbon and martensitic steel. The galvanic behavior between the martensite and ferrite phases favors selective corrosion in the ferrite phase when it is in a NaCl solution [28]. In AHSSs, galvanic corrosion is expected, due to each phase's susceptibility [29]. On the other hand, a study of the corrosion rate in DP600 and DP800 steels immersed in a 3.5% NaCl solution at room temperature indicated that the corrosion resistance of DP800 steel was higher than DP600 steel, which could be corroborated in

the Nyquist diagrams, and the potentiodynamic curves showed similar corrosion current densities of 12 and 17 $\mu A/cm^2$, respectively [30].

Other authors have found that DP steels with simple non-metallic inclusions, such as manganese sulfides, exhibit low resistance to pitting corrosion in chloride solutions [31–33].

This work aimed to study the corrosion behavior of AHSSs by electrochemical noise using a frequency–time domain analysis with noise impedance (Z_n), wavelet decomposition, Hilbert–Huang analysis, and recurrence plots (RP). The steels were tested in different chlorides, namely $MgCl_2$, NaCl, and $CaCl_2$. Microstructural characterization was performed by scanning electron microscopy. AHSSs are used in the automotive industry in environments with a lot of snow and de-icing salts.

2. Materials and Methods

2.1. Materials

The most common AHSS grades in commercial use today are ferritic–bainitic (FB) and dual-phase (DP) steels, which were given the designations FB780 (Yield Strength (YS) = 780 MPa) for a ferrite–bainite microstructure and DP780 (YS = 780 MPa) for a ferrite–martensite microstructure. The chemical compositions of the DP and FB AHSSs utilized in this study, as determined by X-ray fluorescence (Olympus DELTA XRF, Houston, TX, USA), are listed in Table 1.

Table 1. Chemical composition of different AHSS (wt.%).

Element	DP780	FB780
Fe	Balance	Balance
C	0.10	0.09
Mn	2.61	1.73
Cr	0.420	0.640
Mo	-	0.006
Si	0.510	0.300
Ti	0.080	0.021

2.2. Microstructural Characterization

The samples of the AHSSs were prepared using the metallography technique [34], using different SiC grit papers until grades of 4000 were achieved. An alumina suspension of 0.1 μm was used to obtain the microstructure. A five-weight percent Nital solution was used to etch the samples chemically. Lastly, a secondary electron (SE) detector was used to investigate the samples' microstructures by scanning electron microscopy (SEM, JEOL-JSM-5610LV, Tokyo, Japan) at a magnification of 2000×. In order to test for electrochemical corrosion, AHSS samples were ground to 800-grit SiC paper.

2.3. Electrochemical Technique

In order to assess the corrosion behavior of various AHSSs in 3.5 weight percent NaCl, 2 weight percent $CaCl_2$, and 2 weight percent $MgCl_2$ solutions, the EN measurements were conducted at room temperature using a standard three-electrode cell, as shown in Figure 3 [two nominally identical specimens were used as the working electrodes (WE1 and WE2) and a saturated calomel electrode as the reference electrode (RE), respectively]. The EN measurements were conducted following ASTM G199-09 [35–38]. A scanning rate of one data point per second was used to measure 1024 data points in each trial. A Gill-AC potentiostat/galvanostat/ZRA (Zero Resistance Ammeter) from ACM Instruments (Manchester, UK) was used to record the EN measurements simultaneously. The measurements were carried out twice.

A program developed in MATLAB 2018a software (Math Works, Natick, MA, USA) was used to handle data analysis obtained from EN measurements. Energy dispersion plots (EDPs) were used in the frequency–time domain analysis, where the original signal (with DC) was subjected to the orthogonal wavelet transform. In order to obtain the intrinsic

functions (IMF) of the EN signal by an empirical decomposition method (EMD), EN analysis with the Hilbert–Huang transform (HHT) was required. Afterward, instantaneous frequencies were shown using a Hilbert spectrum.
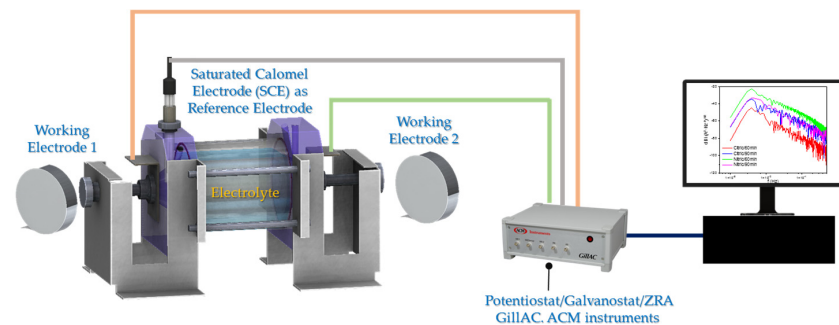

Figure 3. Three-electrode cell for electrochemical noise (EN) measurements.

3. Results and Discussion

3.1. Microstructure

As shown in Figure 4a, hard islands martensite, or bulk martensite, and a soft ferrite phase, or black grains, make up the microstructure of DP780 steel. The average size of the martensite islands ranges from 5 to 55%, and their relative volumes vary accordingly [38–41]. The microstructure of FB780 steel, as shown in Figure 4b, is made up of 30 and 45% fine bainite (bright grains) and soft ferrite matrix (dark grains), with an average grain size of approximately 4 and 2 μm, respectively [42–45].
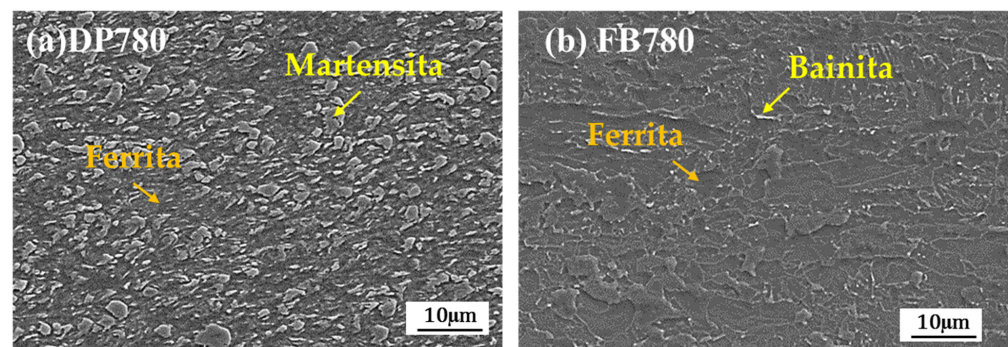
Figure 4. Microstructures of (**a**) DP780 and (**b**) FB780 steels by scanning electron microscopy (SEM).

3.1.1. Noise Impedance

The following formula expresses the noise impedance (Z_n), also known as spectral noise resistance [46,47]:

$$Z_n = \sqrt{\frac{\psi_V(f)}{\psi_I(f)}} \tag{1}$$

The PSD division of potential and current square root calculates Z_n. The electrochemical noise impedance zero (Z_n0) is related to the corrosion resistance [47].

Figure 5 shows the noise impedance graphic (Z_n) of an DP780 alloy exposed in the different electrolytes. The alloy shows similar behavior in the three electrolytes. However, the alloy exposed to NaCl exhibited higher corrosion resistance with a Z_n0 value of 918 $\Omega \cdot cm^2$ (see Table 2). On the other hand, the alloy exposed to $MgCl_2$ presented the lowest Z_n0 value, with 441 $\Omega \cdot cm^2$, indicating that the alloy presents faster corrosion degradation in this medium. The DP780 obtained a value of 825 $\Omega \cdot cm^2$ exposed to $CaCl_2$, indicating that its corrosion resistance is like that of NaCl.
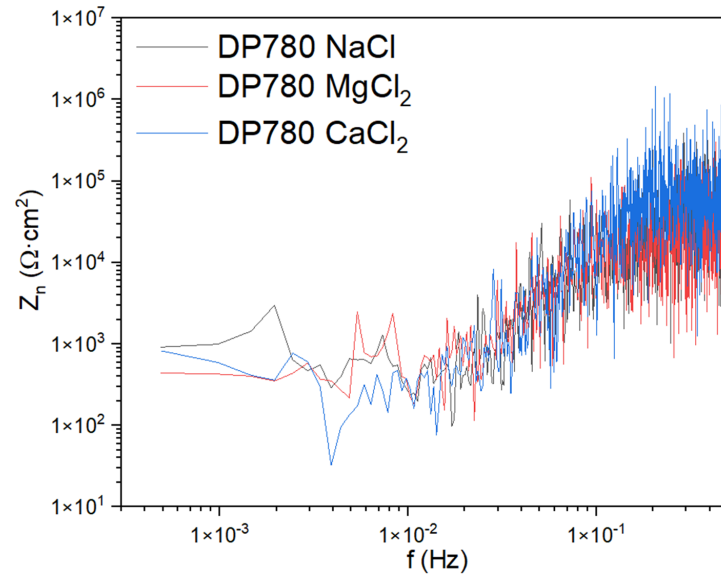
Figure 5. Noise impedance (Z_n) for DP780 in different electrolytes.

Table 2. Noise impedance parameters.

Alloy	Electrolyte	Z_n0 ($\Omega \cdot cm^2$)
DP780	NaCl	918 ± 24
	$MgCl_2$	441 ± 16
	$CaCl_2$	825 ± 28
FB780	NaCl	409 ± 21
	$MgCl_2$	502 ± 14
	$CaCl_2$	432 ± 17

Figure 6 shows the noise impedance of the FB780 alloy in different electrolytes. In this graphic, the FB780 exposed to $MgCl_2$ presented a different behavior; at high frequencies, the Z_n values did not change; however, when exposed to NaCl and CaCl2, the Z_n values increased at high frequencies. That behavior can be related to a more uniform corrosion process that occurs on the surface. Furthermore, the FB780 exposed to $MgCl_2$ presented the highest Z_n0 values of FB780 samples with 502 $\Omega \cdot cm^2$. In contrast, when FB780 was exposed to NaCl, the Z_n0 value was 409 $\Omega \cdot cm^2$.

Figure 6. Noise impedance (Z_n) for FB780 in different electrolytes.

3.1.2. Time-Domain Analysis

Wavelets

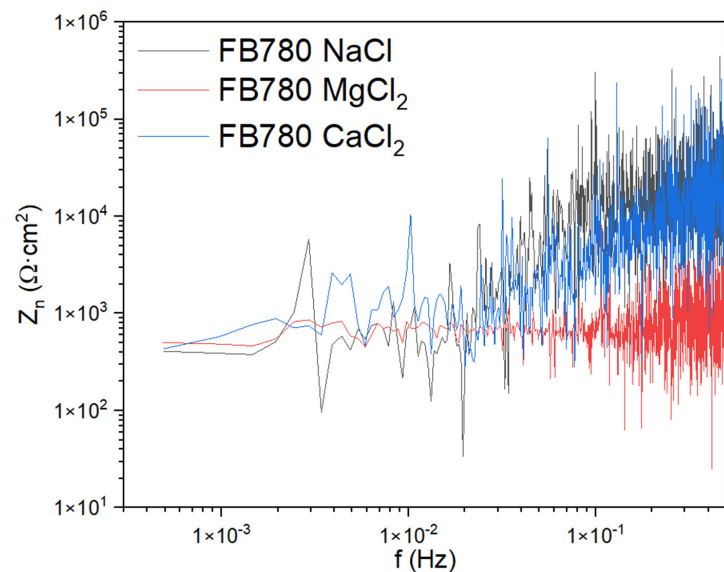A high–low filter is used with wavelets to separate a signal; high frequencies are called details and low frequencies are approximations [45]. An N number of the data's total energy can be found using Equation (2) [47].

$$E = \sum_{n-1}^{N} x_n^2 \tag{2}$$

Additionally, Equation (3) provides the energy fractions of the details and approximations:

$$ED_j^d = \frac{1}{E} \sum_{n=1}^{N} d_{j,n}^2 \quad ED_j^s = \frac{1}{E} \sum_{n=1}^{N} s_{j,n}^2 \tag{3}$$

The total energy evaluated is equal to the energy of each wavelet transform component, according to Equation (4):

$$E = ED_j^s \sum_{j=1}^{j} ED_j^d \tag{4}$$

The authors linked the initial crystal energy, D1 to D3, to metastable pitting. While D7 and D8 are connected to diffusion or regulated processes (uniform corrosion), the crystals D4 through D6 are linked to localized corrosion [48,49].

Figure 7 shows the energy dispersion plot for the DP780 alloy in the different electrolytes. DP780 showed energy accumulation from the D5 crystal, indicating that localized attacks were beginning. Moreover, the major amount of energy is accumulated in crystals D7 and D8, indicating that a uniform corrosion process is presented. This behavior is associated with a uniform pitting attack on the alloy surface.
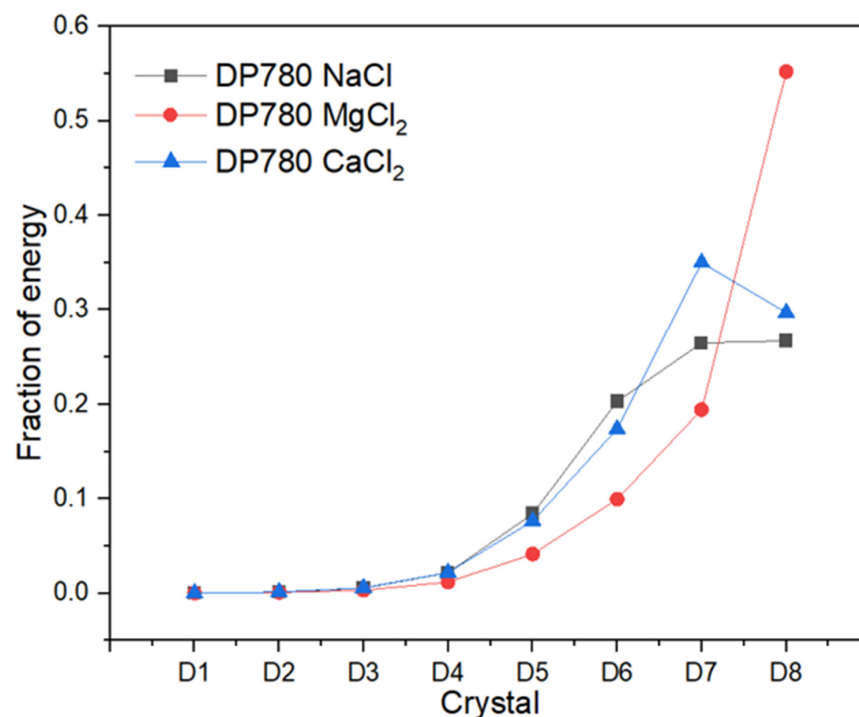

Figure 7. Energy dispersion plot of DP780 alloy.

Figure 8 shows the energy dispersion plot for the FB780 alloy in different electrolytes. FB780 exposed to NaCl and CaCl$_2$ presented a similar behavior to DP780 alloys, with energy accumulation at the D5 and D6 crystals, indicating that localized processes were

occurring on metal surfaces. In addition, the energy accumulation at the D7 and D8 crystals is associated with uniform corrosion provoked by a uniform pitting distribution.
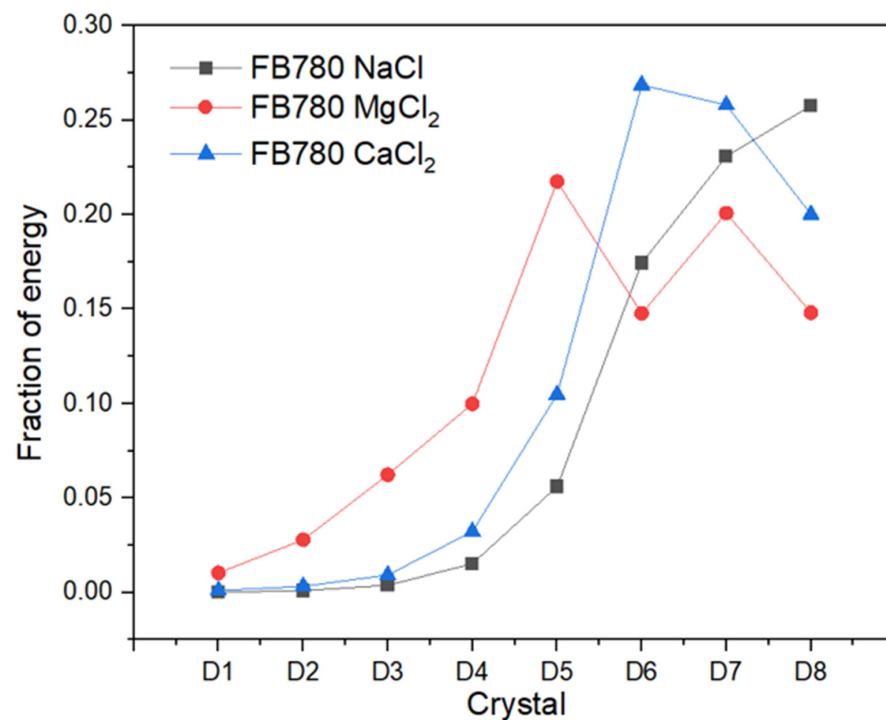

Figure 8. Energy dispersion plot of FB780 alloy.

Recurrence Plots and Hilbert–Huang Transform

Recurrence plots are a useful tool for non-linear system analysis. Various methodologies must be used to assess the type and progress of corrosion on the surface because corrosion is a chaotic and non-linear system. An effective method for obtaining that analysis is RPs.

Recurrence plots are time-function-realized, two-dimensional graphs. The path of x_i in R_m, where m is the spatial dimension, is given to I and j at a time interval of ε. The times t_i and t_j from two dimensions are displayed as a two-dimensional square matrix by the RP. The matrix is displayed in Equation (5) [50–53]:

$$R_{ij}(\varepsilon) = \Theta\left(\varepsilon - \left\|\vec{x}_i - \vec{x}_j\right\|\right),\ i, j = 1, \ldots, N \tag{5}$$

where $||.||$ is the norm (Euclidean, maximum, or Manhattan), μ is the distance umbral, $\Theta(x)$ is the Heaviside function, and N is the number of data or points x_i. Equation (4) illustrates the recurrence rate, which determines the recurrence density:

$$RR(\varepsilon) = \frac{1}{N^2} \sum_{i,\,j=1}^{N} R_{i,\,j} \tag{6}$$

In an umbral zone, the recurrence rate (RR) indicates the likelihood of reconstructing a single track.

The diagonal lines of the RP show the system's determinism and how the trajectory has changed over time in the phase space. The determinism (DET) is computed using the following equation:

$$DET = \frac{\sum_{l=l_{min}}^{N} l\, p(l)}{\sum_{l=1}^{N} l\, p(l)} \tag{7}$$

Long diagonal lines on the RP are necessary for periodicity, and DET approaches unity; stochastic signals result in solitary dots, which restricts DET to values near zero. The average diagonal line length (L), another RQA metric associated with diagonal lines, is depicted as follows in Equation (8):

$$L = \frac{\sum_{l=l_{max}}^{N} l \, p(l)}{\sum_{l=lmin}^{N} p(l)} \tag{8}$$

TT gives the average length of the vertical structures and indicates the average time the system spends in a given condition (as indicated by the number of recurrence points); see Equation (9).

$$TT = \frac{\sum_{v=v_{min}}^{N} v \, P(v)}{\sum_{v=vmin}^{N} P(v)} \tag{9}$$

The electrochemical phenomenon that takes place throughout the corrosion process is described by the electrochemical noise (EN) technique. The Hilbert–Huang analysis is one methodology used to describe the EN method. This technique facilitates the frequency and timing of energy exchanges; the energy, known as instantaneous energy, is derived from the signal's inherent function and is retrieved by signal decomposition [54–56]. Equation (10) explains the empirical method of decomposition (EMD):

$$x(t) = \sum_{i=1}^{N} h^{(i)}(t) + d(t) \tag{10}$$

where $d(t)$ is the average of the trend at a low frequency of the time series $x(t)$ and cannot be decomposed; $h^{(i)}(t)$ is the i-th term of IMF that is generated; these numbers must satisfy the conditions that the extreme and cross numbers are equal or differ by a maximum of 1 and that each point using the local maximum and minimum must be 0. The HHT is represented by Equation (11):

$$y_j(t) = \frac{1}{\pi} p \int_{-\infty}^{\infty} \frac{h_j(\tau)}{t - \tau} d\tau \tag{11}$$

where p is connected to the Cauchy principle and is associated with an average of IMF; $y_j(t)$ is the Hilbert transform, and IMF is represented by h_j.

Figure 6 shows the signal analysis results by RPs and HHT, comparing the results with optical microscopy. Figure 9a shows the graphics of DP780 exposed to NaCl, where the RP showed a high determinist behavior with a value of 0.9769 (see Table 3) and RR of 0.0562. The RP presents some blue points in the graphics, indicating that a process occurs at that time. It can be related to the energy presented at middle frequencies in the Hilbert specter. That behavior is associated with localized corrosion; however, the high DET value (indicating a uniform process) can be related to the corrosion process in the material; a galvanic couple occurs in the superficies of dual-phase alloy. The dominance of uniform process that occurs in a surface is related to the corrosion process that consists of the diffusion of ions on the metal surface, that attacks in specific zones (the more susceptible phase), generating localized attacks (energy at middle frequencies and blue zones in RP) that generate a uniform pitting attack. Finally, the localized attack occurs in the ferrite phase. All the DP780 samples from Figure 9a–c show this behavior. Figure 9c shows a similar behavior with a high DET value (0.9844). It can be related to oxygen diffusion, so the microscopy shows a highly corroded area; however, when zoomed in to a microscopic level, it can be observed how the corrosion is occurring in preference zones (ferrite), being governed by the process described previously.

Figure 10 shows the results of FB780 alloy exposed to the different electrolytes. Figure 10a,c show similar behavior in DP780, indicating that a uniform process occurs on the surface. However, the uniform process from the surface will attack preferent zones, principally ferrite zones. For that reason, in the Hilbert specter, energy is accumulated

at the beginning of the time period at low frequencies due to ion diffusion in the metal surface. However, after some exposure time, energy begins to appear at middle frequencies, indicating that localized processes are occurring, and due to the galvanic couple in ferrite zones, the attacks will be uniform after some time.
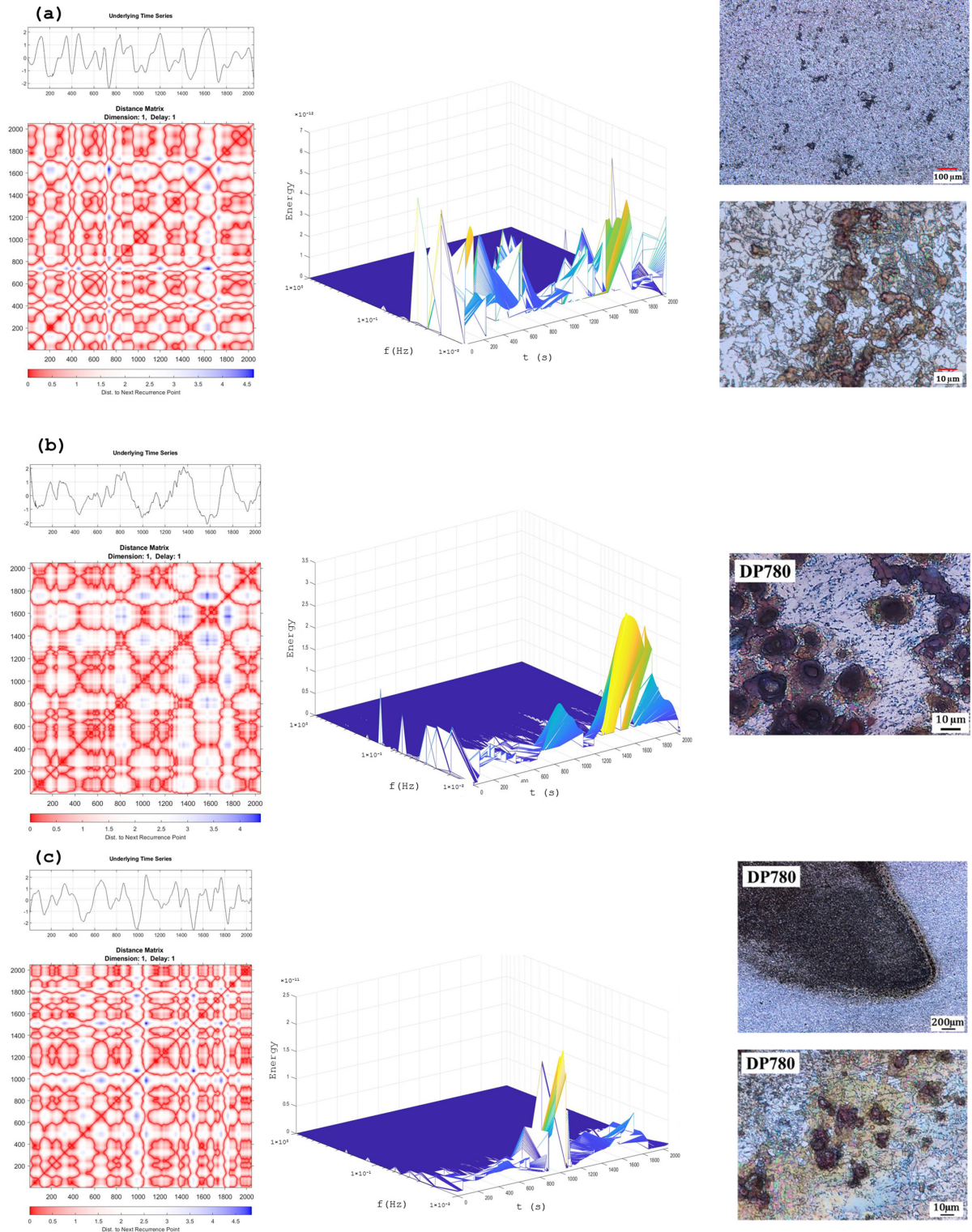
Figure 9. Recurrence plots, Hilbert specter, and microscopy analysis for DP780 exposed to (**a**) NaCl, (**b**) MgCl$_2$, and (**c**) CaCl$_2$.

Table 3. Recurrence plots parameters.

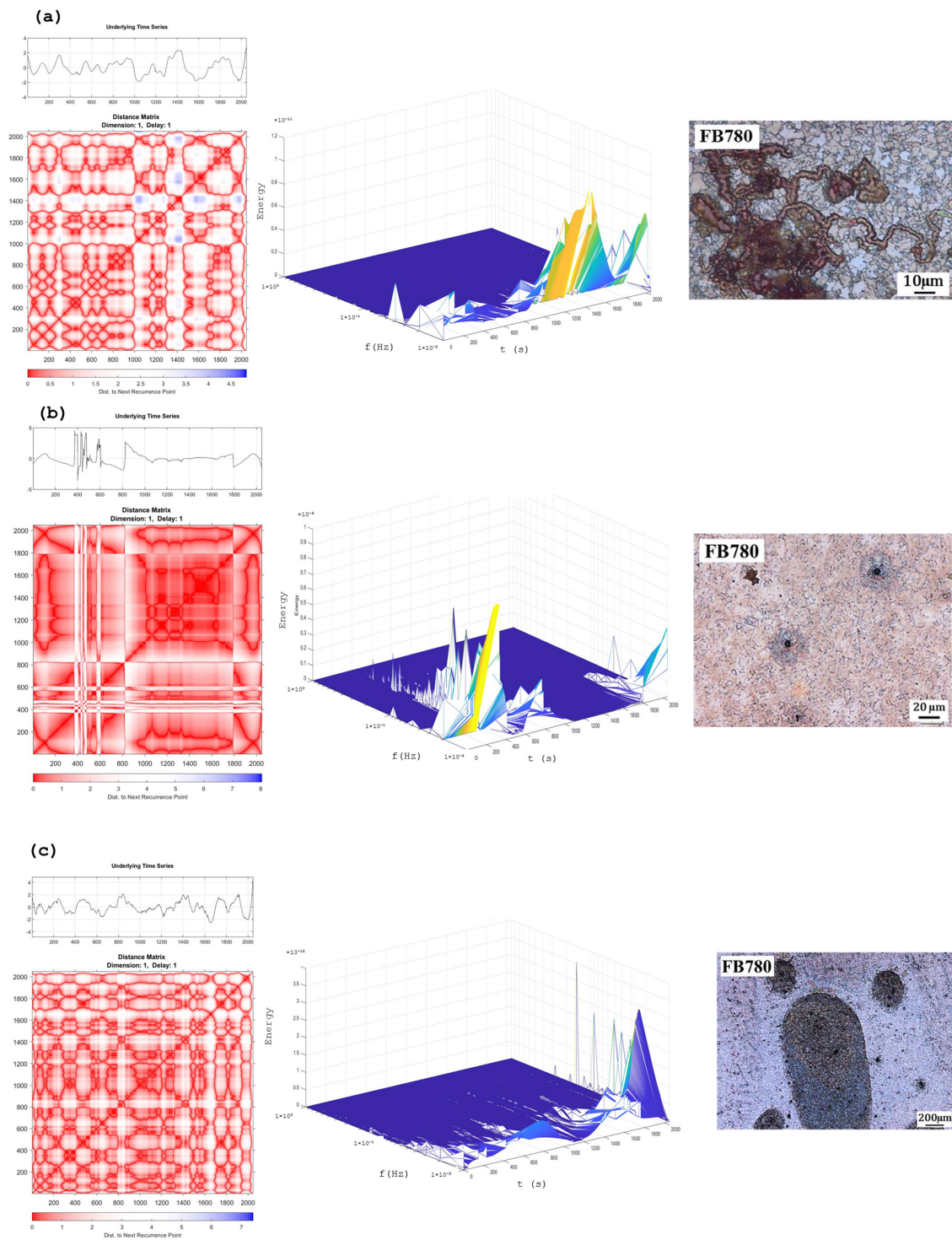| Alloy	Electrolyte	RR	DET	L	TT
DP780	NaCl	0.0562 ± 0.0002	0.9769 ± 0.001	5.06 ± 0.02	6.51 ± 0.05
	$MgCl_2$	0.0592 ± 0.0001	0.9831 ± 0.0002	6.28 ± 0.09	8.16 ± 0.09
	$CaCl_2$	0.0589 ± 0.0004	0.9844 ± 0.0004	5.04 ± 0.005	6.48 ± 0.07
FB780	NaCl	0.0593 ± 0.0002	0.987 ± 0.0008	6.26 ± 0.008	8.12 ± 0.05
	$MgCl_2$	0.0823 ± 0.0001	0.9391 ± 0.0001	10.07 ± 0.03	13.92 ± 0.2
	$CaCl_2$	0.06 ± 0.004	0.9142 ± 0.0001	4.17 ± 0.08	5.45 ± 0.03

Figure 10. Recurrence plots, Hilbert specter, and microscopy analysis for FB780 exposed to (**a**) NaCl, (**b**) $MgCl_2$, and (**c**) $CaCl_2$.

In contrast, Figure 10b shows a localized process; in this case, the value of RR increases to 0.0823 (in comparison with the other values between 0.05 and 0.06). Also, L and T's values are higher than those obtained in the other samples (10.07 and 13.92); those values are related to the time of recurrence point occurrence. The recurrence points are related to the localized process, and a high value of these two parameters indicates the localization process.

4. Discussion

Two basic reactions dominate the corrosion process:

$$\text{Fe} \rightarrow \text{Fe}^{2+} + 2\text{e}^- \tag{12}$$

$$\text{O}_2 + 2\text{H}_2\text{O} + 4\text{e}^- \rightarrow 4\text{OH}^- \tag{13}$$
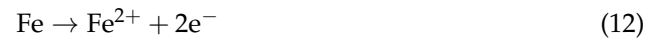
Those reactions generate an active oxidation; when oxygen is diffused on the surface, the corrosion products generated are porous and do not give passivation to the surface. That facilitates the attack of Cl^- ions on the ferrite phase, generating a localized attack and avoiding the passivation of surface-generating pitting in the ferrite zone [57,58]. The following reactions govern the chemical reaction:

$$\text{Fe}^{2+} + \text{Cl}^- \rightarrow \text{FeCl}_2 \tag{14}$$

$$\text{FeCl}_2 + \text{H}_2\text{O} \rightarrow \text{Fe(OH)}_2 + 2\text{Cl}^- \tag{15}$$

This alloy type's corrosion process depends on the metal matrix's metallurgical heterogeneities and the passive layer's absence [58,59]. The presence of cathodic and anodic zones due to the difference in phases, grain variations, and impurities, and the lack of homogeneity is conducive to localized attacks. For these alloys, the phase difference generates galvanic corrosion [60].

The cathode role of bainite and martensite, due to the oxygen reception, made ferrite act as an anode due to the low presence of O_2, making it susceptible to OH^- and Cl^- attacks [61].

The dissolution process was generated in uniform form in ferrite, so the results of RPs and HHT presented high activity at low frequencies, which was conducive to initiating some localized attacks. Also, some authors consider that the corrosion process in this class of alloys is not only for the galvanic couple; it can be generated by an auto-corrosion of the only phase in double-phase steels [62–64].

The corrosion mechanism of DP780 and FB780 presented previously can be complemented with a uniform dissolution of the area when exposed to CaCl_2. This occurs due to the effect of the solution in ferrite, martensite, and bainite, generating a galvanic couple through an auto-corrosion process. The ferrite dissolution provoked active zones, and the uniformly distributed pitting was connected, generating a uniform dissolution of material, as shown in Figure 11 [64,65]. Therefore, the RPs and HHT showed high energy accumulation at middle and high frequencies due to localized processes (at middle and high frequencies) that provoke uniform attacks (at high frequencies).

The corrosion behavior of FB780 steel with a ferrite–bainite microstructure in CaCl_2 and MgCl_2 solutions presents localized corrosion, where the bainite phase dissolved faster than the ferrite phase because it acted as an anode. The iron carbides (green dots) acted as cathodes, as Figure 10a indicated. The disintegration process of ferrite–martensite DP780 steel in test solutions is depicted in Figure 10b. Because it functions as a cathode, martensite acts as a barrier to corrosion, and the continuous ferrite-phase matrix restricts the spread of corrosion.

In the case of ferrite–bainite DP, the microstructure influences the corrosion initiation of the Cr-Mo alloyed steel. Zones with low Cr-Mo content generates more crystal defects, decreasing the potential and increasing the susceptibility of microgalvanic corrosion. The

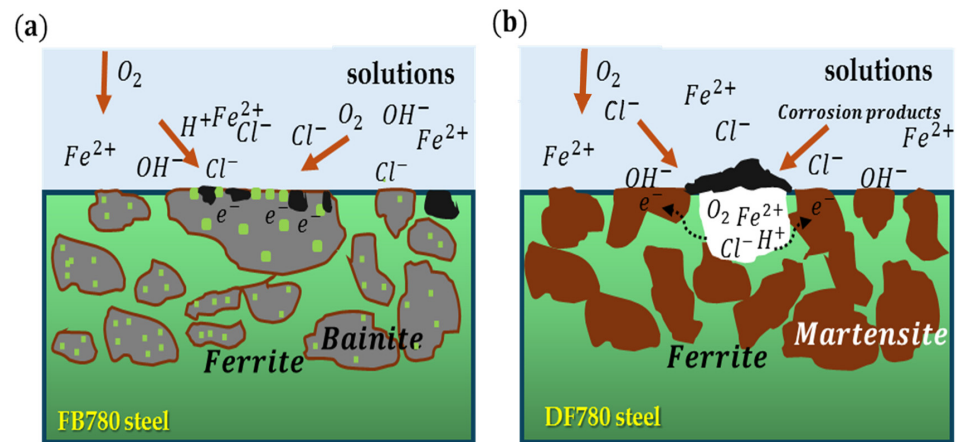ferrite phase works as a cathode for a higher Cr-Mo concentration, and the bainite is dissolved [65–68].

Figure 11. Schematic representation of corrosion in (**a**) ferrite–bainite FB780 steel/CaCl$_2$-MgCl$_2$, (**b**) dual-phase DP780 steel/test solutions.

It is important to mention the aggression of Cl$^-$ ions; in several research studies, different alloys have been exposed to this medium, demonstrating that Cl$^-$ will attack the more susceptible zones, provoking localized corrosion in this part and generating a more aggressive attack. It can be observed with energy at the middle crystals in a wavelets analysis or at middle frequencies in the HHT studies [69–73]. For these alloys, the attacks began at the ferrite-phase or inclusion zones; authors such as Macdonald [73–76] describe this phenomenon with the point defect model, indicating that the passive layer generated on a material surface presents defects of cation and oxygen vacancies generating and annihilating the metal/film and film/solution interfaces, being a similar process to high-temperature oxidation. FB steel shows a higher corrosion kinetic due to the ferritic phase matrix; as it is more present in the material, the anode is higher, and corrosion resistance decreases.

Due to the non-linear signal characteristics, the analysis by methods such as wavelets, HHT, and RPs are crucial in these complex systems. This research showed that a non-conventional EN analysis is helpful to determine the attacks in galvanic couples, supporting wavelets with HHT and RPs methods. It is possible to analyze the changes in the corrosion process within the time, and not only with a scalar aspect, as in conventional methods. With the HHT and RPs methods, it was possible to determine the moment of pitting attack and nucleations. Also, when only localized corrosion was present, it could be identified with these methods [77–89].

However, with wavelets, HHT, and RPs, it is not possible to determine the corrosion resistance of a material; for that reason, it is important to complement with a noise impedance analysis (Z$_n$) due to the certainty of this analysis in determining the corrosion resistance. With this analysis, it was possible to determine the high corrosion resistance of DP780 in comparison to FB780 in the different electrolytes.

5. Conclusions

DP780 and FB780 presented a galvanic couple with an auto-corrosion process on the surface. The corrosion process is generated by an ion diffusion in the surface (a uniform process) that attacks specific zones such as ferrite, inclusions, or some defects (localized process) and mitigates the attack of Cl$^-$ that dissolves the ferrite phase uniformly, connecting the pitting distributed in a uniform way and dissolving the surface.

Wavelets, RPs, and HHT help identify the corrosion process that occurs on the surface. The RPs help to find the recurrence zones where some localized attacks (galvanic coupling)

occur; in this case, the blue zones of the RPs indicate the uniform attacks generated by the dissolution of the material.

The presence of inclusions influences the beginning of localized attacks.

The Z_n parameter showed that DP780 presented a higher corrosion resistance (918 $\Omega \cdot cm^2$ and 825 $\Omega \cdot cm^2$) than FB780 exposed to NaCl and $CaCl_2$. However, DP780 presented a lower noise impedance when exposed to $MgCl_2$ (441 $\Omega \cdot cm^2$).

Parameters such as L (diagonal line) and TT (the average length of the vertical structures) help determine the corrosion type on the material's surface. A high value of these parameters is related in this research to localized corrosion, indicating the time associated with the change in one process, as presented with FB780 exposed to $MgCl_2$ (10.07 and 13.92). As the uniform process occurs constantly, the TT value is going to be lower (4.17–6.2).

Author Contributions: Conceptualization, F.A.-C., M.M.-R. and C.G.-T., methodology, M.M.-R., F.E.-L., E.M.-B., M.L.-B., J.M.J.-M. and L.L.-R. data curation, F.A.-C., L.L.-R., D.N.-M., F.A.-C. M.A.B.-Z. and F.E.-L.; formal analysis, F.A.-C., C.G.-T., M.M.-R., E.M.-B., M.A.B.-Z., L.L.-R., D.N.-M., M.L.-B. and C.G.-T.; writing—review and editing, F.A.-C., J.M.J.-M. and C.G.-T. All authors have read and agreed to the published version of the manuscript.

Data Availability Statement: The raw data supporting the conclusions of this article will be made available by the authors on request.

Conflicts of Interest: The authors declare no conflicts of interest.

References

1. Tamarelli, C.M. AHSS 101: The evolving use of advanced high-strength steel for automotive applications. *Steel Mark. Dev. Inst.* **2011**, *1*, 42.
2. Montoya-Rangel, M.; de Garza-Montes, O.N.; Gaona-Tiburcio, C.; Colás, R.; Cabral-Miramontes, J.; Nieves-Mendoza, D.; Maldonado-Bandala, E.; Chacón-Nava, J.; Almeraya-Calderón, F. Electrochemical noise measurements of advanced high-strength steels in different solutions. *Metals* **2020**, *10*, 1232. [CrossRef]
3. Keeler, S.; Kimchi, M. *Advanced High-Strength Steels Application Guidelines Version 5.0*; WorldAutoSteel: Brussels, Belgium, 2014.
4. Available online: https://www.energy.gov/eere/vehicles/articles/autosteel-partnership-ahss-stamping-strain-rate-characterization-sheet-steel (accessed on 15 October 2024).
5. Galán, J.; Samek, L.; Verleysen, P.; Verbeken, K.; Houbaert, Y. Advanced high strength steels for automotive industry. *Rev. Metal.* **2012**, *48*, 118–131. [CrossRef]
6. Maffei, B.; Salvatore, W.; Valentini, R. Dual-phase steel rebars for high-ductile r.c. structures, Part 1: Microstructural and mechanical characterization of steel rebars. *Eng. Struct.* **2007**, *29*, 3325–3332. [CrossRef]
7. Khan, A.S.; Baig, M.; Choi, S.H.; Yang, H.S.; Sun, X. Quasi-static and dynamic responses of advanced high strength steels: Experiments and modeling. *Int. J. Plast.* **2012**, *30–31*, 1–17. [CrossRef]
8. Kumar, A.; Singh, S.B.; Ray, K.K. Influence of bainite/martensite-content on the tensile properties of low carbon dual-phase steels. *Mater. Sci. Eng. A* **2008**, *474*, 270–282. [CrossRef]
9. Qu, S.; Zhang, Y.; Pang, X.; Gao, K. Influence of temperature field on the microstructure of low carbon microalloyed ferrite-bainite dual-phase steel during heat treatment. *Mater. Sci. Eng. A* **2012**, *536*, 136–142. [CrossRef]
10. Lesch, C.; Kwiaton, N.; Klose, F.B. Advanced High Strength Steels (AHSS) for Automotive Applications −Tailored Properties by Smart Microstructural Adjustments. *Steel Res. Int.* **2017**, *88*, 1700210. [CrossRef]
11. Mintz, B. Hot dip galvanising of transformation induced plasticity and other intercritically annealed steels. *Int. Mater. Rev.* **2001**, *46*, 169–197. [CrossRef]
12. Uzun, H.; Önal, E. Mechanical Properties and Corrosion Behaviors in 3.5% NaCl Solution of Grade-A and Dual-Phase Steels Welded by FCAW. *Period. Eng. Nat. Sci.* **2013**, *1*, 25–32. [CrossRef]
13. Abedini, O.; Behroozi, M.; Marashi, P.; Ranjbarnodeh, E.; Pouranvari, M. Intercritical heat treatment temperature dependence of mechanical properties and corrosion resistance of dual phase steel. *Mater. Res.* **2019**, *22*, e20170969. [CrossRef]
14. Schmitta, J.H.; Iungb, T. New developments of advanced high-strength steels for automotive applications. *Comptes Rendus. Phys.* **2018**, *19*, 641–656. [CrossRef]
15. Keleştemur, O.; Yildiz, S. Effect of various dual-phase heat treatments on the corrosion behavior of reinforcing steel used in the reinforced concrete structures. *Constr. Build. Mater.* **2009**, *23*, 78–84. [CrossRef]

16. Billur, E.; Karabulut, S.; Yılmaz, İ.Ö.; Erzincanlıoğlu, S.; Çelik, H.; Altınok, E.; Başer, T. Mechanical Properties of Trip Aided Bainitic Ferrite TBF Steels in Production and Service Conditions. *Hittite J. Sci. Eng.* **2018**, *5*, 231–237. [CrossRef]

17. Montoya-Rangel, M.; Garza-Montes-de-Oca, N.F.; Gaona-Tiburcio, C.; Almeraya-Calderón, F. Corrosion mechanism of advanced high strength dual-phase steels by electrochemical noise analysis in chloride solutions. *Mater. Today Commun.* **2023**, *35*, 105663. [CrossRef]

18. Wang, Y.; Zuo, X.; Li, J. Corrosion Resistance of the Welded Joint of Submarine Pipeline Steel with Ferrite Plus Bainite Dual-Phase Microstructure. *Steel Res. Int.* **2015**, *86*, 1260–1270. [CrossRef]

19. Wang, Z.F.; Li, P.H.; Guan, Y.; Chen, Q.F.; Pu, S.K. The corrosion resistance of ultra-low carbon bainitic steel. *Corros. Sci.* **2009**, *51*, 954–961. [CrossRef]

20. Mehdipour, M.; Naderi, R.; Markhali, B.P. Electrochemical study of effect of the concentration of azole derivatives on corrosion behavior of stainless steel in H_2SO_4. *Prog. Org. Coat.* **2014**, *77*, 1761–1767. [CrossRef]

21. Xia, D.; Song, S.; Wang, J.; Shi, J.; Bi, H.; Gao, Z. Determination of corrosion types from electrochemical noise by phase space reconstruction theory. *Electrochem. Commun.* **2012**, *15*, 88–92. [CrossRef]

22. Monticelli, C. Evaluation of Corrosion Inhibitors by Electrochemical Noise Analysis. *J. Electrochem. Soc.* **1992**, *139*, 706. [CrossRef]

23. Almeraya-Calderón, F.; Jáquez-Muñoz, J.M.; Maldonado-Bandala, E.; Cabral-Miramontes, J.; Nieves-Mendoza, D.; Olgui-Coca, J.; Lopez-Leon, L.D.; Estupiñán-López, F.; Lira-Martínez, A.; Gaona Tiburcio, C. Corrosion Resistance of Titanium Alloys Anodized in Alkaline Solutions. *Metals* **2023**, *13*, 1510. [CrossRef]

24. Suresh, G.U.; Kamachi, M.S. Electrochemical Noise Analysis of Pitting Corrosion of Type 304L Stainless Steel. *Corrosion* **2014**, *70*, 283–293. [CrossRef] [PubMed]

25. Homborg, A.M.; Cottis, R.A.; Mol, J.M.C. An integrated approach in the time, frequency and time-frequency domain for the identification of corrosion using electrochemical noise. *Electrochim. Acta* **2016**, *222*, 627–640. [CrossRef]

26. Mansfeld, F.; Sun, Z. Technical Note: Localization Index Obtained from Electrochemical Noise Analysis. *Corrosion* **1999**, *55*, 915–918. [CrossRef]

27. Nagiub, A.M. Electrochemical Noise Analysis for Different Green Corrosion Inhibitors for Copper Exposed to Chloride Media. *Corros. Sci.* **2017**, *35*, 201–210. [CrossRef]

28. Ikpeseni, S.C.; Ameh, E.S. Effect of Temperature and Microstructure on the Corrosion Behaviour of a low Carbon Dual Phase Steel. *Am. J. Eng. Res.* **2017**, *6*, 01–07.

29. Si, Y. Investigation of Galvanic Corrosion Behavior of Dual Phase Steel. *ECS Trans.* **2016**, *72*, 13. [CrossRef]

30. Fushimi, K.; Yanagisawa, K.; Nakanishi, T.; Hasegawa, Y.; Kawano, T.; Kimura, M. Microelectrochemistry of dual-phase steel corroding in 0.1 M sulfuric acid. *Electrochim. Acta* **2013**, *114*, 83–87. [CrossRef]

31. Gerengi, H.; Sen, N.; Uygur, I.; Kaya, E. Corrosion behavior of dual phase 600 and 800 steels in 3.5 wt.% NaCl environment. *J. Adhes. Sci. Technol.* **2020**, *34*, 903–915. [CrossRef]

32. Park, I.J.; Kim, S.T.; Lee, I.S.; Park, Y.S.; Moon, M.B. A study on corrosion behavior of DP-type and TRIP-type cold rolled steel sheet. *Mater. Trans.* **2009**, *50*, 1440–1447. [CrossRef]

33. Park, I.J.; Lee, S.M.; Kang, M.; Lee, S.; Lee, Y.K. Pitting corrosion behavior in advanced high strength steels. *J. Alloys Compd.* **2015**, *619*, 205–210. [CrossRef]

34. *ASTM E3-95*; Standard Practice for Preparation of Metallographic Specimens. ASTM International: West Conshohocken, PA, USA, 2007.

35. *ASTM G199-09*; Standard Guide for Electrochemical Noise Measurement. ASTM International: West Conshohocken, PA, USA, 2014.

36. Jáquez-Muñoz, J.M.; Gaona-Tiburcio, C.; Méndez-Ramírez, C.T.; Baltazar-Zamora, M.Á.; Estupinán-López, F.; Bautista-Margulis, R.G.; Cuevas-Rodríguez, J.; Flores-De los Rios, J.P.; Almeraya-Calderón, F. Corrosion of Titanium Alloys Anodized Using Electrochemical Techniques. *Metals* **2023**, *13*, 476. [CrossRef]

37. Jáquez-Muñoz, J.M.; Gaona-Tiburcio, C.; Méndez-Ramírez, C.T.; Martínez-Ramos, C.; Baltazar-Zamora, M.A.; Santiago-Hurtado, G.; Estupinan-Lopez, F.; Landa-Ruiz, L.; Nieves-Mendoza, D.; Almeraya-Calderon, F. Electrochemical Noise Analysis: An Approach to the Effectivity of Each Method in Different Materials. *Materials* **2024**, *17*, 4013. [CrossRef] [PubMed]

38. Almeraya-Calderon, F.; Villegas-Tovar, M.; Maldonado-Bandala, E.; Lara-Banda, M.; Baltazar-Zamora, M.A.; Santiago-Hurtado, G.; Nieves-Mendoza, D.; Lopez-Leon, L.D.; Jaquez-Muñoz, J.M.; Estupiñán-López, F.; et al. Use of Electrochemical Noise for the Study of Corrosion by Passivated CUSTOM 450 and AM 350 Stainless Steels. *Metals* **2024**, *14*, 341. [CrossRef]

39. Thewlis, G. Classification and quantification of microstructures in steels. *J. Mater. Sci. Technol.* **2004**, *20*, 143–160. [CrossRef]

40. Kang, Y.; Han, Q.; Zhao, X.; Cai, M. Influence of nanoparticle reinforcements on the strengthening mechanisms of an ultrafine-grained dual phase steel containing titanium. *Mater. Des.* **2013**, *44*, 331–339. [CrossRef]

41. Martínez-Villafañe, A.; Almeraya-Calderón, F.; Gaona-Tiburcio, C.; Gonzalez-Rodriguez, J.; Porcayo-Calderón, J. High-Temperature Degradation and Protection of Ferritic and Austenitic Steels in Steam Generators. *J. Mater. Eng. Perform.* **1998**, *7*, 108–113. [CrossRef]

42. Martínez-Aparicio, B.; Gaona-Tiburcio, C.; Almeraya-Calderon, F.; Goldsberry, R.; Castaneda, H. Evaluation of Passive Films on 17-7PH and 410 Stainless Steel Exposed to NaCl Solution. *Materials* **2024**, *17*, 4060. [CrossRef]

43. Kwon, O.; Lee, K.; Kim, G.; Chin, K.-G. New Trends in Advanced High Strength Steel Developments For Automotive Application. *Mat. Sci. Forum.* **2010**, *638–642*, 136–141. [CrossRef]

44. Aydin, K.; Essadiqi, E.; Yue, S. Development of 3rd generation AHSS with medium Mn content alloying compositions. *Mater. Sci. Eng. A.* **2013**, *564*, 501–508. [CrossRef]

45. Saeidi, N.; Ekrami, A. Comparison of mechanical properties of martensite/ferrite and bainite/ferrite dual phase 4340 steels. *Mater. Sci. Eng. A* **2009**, *523*, 125–129. [CrossRef]

46. Homborg, A.M.; Oonincx, P.J.; Mol, J.M.C. Wavelet Transform Modulus Maxima and Holder Exponents Combined with Transient Detection for the Differentiation of Pitting Corrosion Using Electrochemical Noise. *Corrosion* **2018**, *74*, 1001–1010. [CrossRef] [PubMed]

47. Brockwell, P.J.; Davis, R.A. *Introduction to Time Series and Forecasting*; Springer: Cham, Switzerland, 2016. [CrossRef]

48. Cai, C.; Zhang, Z.; Cao, F.; Gao, Z.; Zhang, J.; Cao, C. Analysis of Pitting Corrosion Behavior of Pure Al in Sodium Chloride Solution with the Wavelet Technique. *J. Electroanal. Chem.* **2005**, *578*, 143–150. [CrossRef]

49. Homborg, A.M.; van Westing, E.P.M.; Tinga, T.; Zhang, X.; Oonincx, P.J.; Ferrari, G.M.; de Wit, J.H.W.; Mol, J.M.C. Novel Time–Frequency Characterization of Electrochemical Noise Data in Corrosion Studies Using Hilbert Spectra. *Corros. Sci.* **2013**, *66*, 97–110. [CrossRef]

50. Legat, A.; Dolecek, V. Corrosion Monitoring System Based on Measurement and Analysis of Electrochemical Noise. *Corrosion* **1995**, *51*, 295–300. [CrossRef]

51. Coakley, J.; Vorontsov, V.A.; Littrell, K.C.; Heenan, R.K.; Ohnuma, M.; Jones, N.G.; Dye, D. Nanoprecipitation in a Beta-Titanium Alloy. *J. Alloys Compd.* **2015**, *623*, 146–156. [CrossRef]

52. Botona Pedemonte, F.J.; Aballe Villero, A.; Marcos Bárcena, M. *Ruido Electroquímico. Métodos de Análisis*; Septem Ediciones, S.L.: Oviedo, Spain, 2002; ISBN 84-95687-33-X.

53. Martínez-Ramos, C.; Olguin-Coca, J.; Lopez-Leon, L.D.; Gaona-Tiburcio, C.; Lara-Banda, M.; Maldonado-Bandala, E.; Castañeda-Robles, I.; Jaquez-Muñoz, J.M.; Cabral-Miramontes, J.; Nieves-Mendoza, D.; et al. Electrochemical Noise Analysis Using Experimental Chaos Theory, Power Spectral Density and Hilbert–Huang Transform in Anodized Aluminum Alloys in Tartaric–Phosphoric–Sulfuric Acid Solutions. *Metals* **2023**, *13*, 1850. [CrossRef]

54. Cappeln, F.; Bjerrum, N.J.; Petrushina, I.M. Electrochemical Noise Measurements of Steel Corrosion in the Molten NaCl-K[Sub 2]SO[Sub 4] System. *J. Electrochem. Soc.* **2005**, *152*, B228. [CrossRef]

55. Calabrese, L.; Galeano, M.; Proverbio, E. Identifying Corrosion Forms on Synthetic Electrochemical Noise Signals by the Hilbert–Huang Transform Method. *Corros. Eng. Sci. Technol.* **2018**, *53*, 492–501. [CrossRef]

56. Bertocci, U.; Huet, F.; Nogueira, R.P.; Rousseau, P. Drift Removal Procedures in the Analysis of Electrochemical Noise. *Corrosion* **2002**, *58*, 337–347. [CrossRef]

57. Homborg, A.M.; Tinga, T.; Van Westing, E.P.M.; Zhang, X.; Ferrari, G.M.; De Wit, J.H.W.; Mol, J.M.C. A Critical Appraisal of the Interpretation of Electrochemical Noise for Corrosion Studies. *Corrosion* **2014**, *70*, 971–987. [CrossRef] [PubMed]

58. Enestam, S.; Bankiewicz, D.; Tuiremo, J.; Mäkelä, K.; Hupa, M. Are NaCl and KCl equally corrosive on superheater materials of steam boilers? *Fuel* **2013**, *104*, 294–306. [CrossRef]

59. Marcus, P.; Maurice, V.; Strehblow, H.H. Localized corrosion (pitting): A model of passivity breakdown including the role of the oxide layer nanostructure. *Corros. Sci.* **2008**, *50*, 2698–2704. [CrossRef]

60. Shibaeva, T.V.; Laurinavichyute, V.K.; Tsirlina, G.A.; Arsenkin, A.M.; Grigorovich, K.V. The effect of microstructure and non-metallic inclusions on corrosion behavior of low carbon steel in chloride containing solutions. *Corros. Sci.* **2014**, *80*, 299–308. [CrossRef]

61. Shi, Y.Y.; Zhang, Z.; Cao, F.H.; Zhang, J.Q. Dimensional analysis applied to pitting corrosion measurements. *Electrochim. Acta* **2008**, *53*, 2688–2698. [CrossRef]

62. Soleimani, M.; Mirzadeh, H.; Dehghanian, C. Processing Route Effects on the Mechanical and Corrosion Properties of Dual Phase Steel. *Met. Mater. Int.* **2020**, *26*, 882–890. [CrossRef]

63. Jáquez-Muñoz, J.M.; Gaona-Tiburcio, C.; Mendez-Ramirez, C.T.; Carrera-Ramirez, M.G.; Baltazar-Zamora, M.A.; Santiago-Hurtado, G.; Lara-Banda, M.; Estupiñan-Lopez, F.; Nieves-Mendoza, D.; Almeraya-Calderon, F. Corrosion of Anodized Titanium Alloys. *Coatings* **2024**, *14*, 809. [CrossRef]

64. Kumar, S.; Kumar, A.; Vinaya; Madhusudhan, R.; Sah, R.; Manjini, S. Mechanical and Electrochemical Behavior of Dual-Phase Steels Having Varying Ferrite Martensite Volume Fractions. *J. Mater. Eng. Perform.* **2019**, *28*, 3600–3613. [CrossRef]

65. Haisch, T.; Mittemeijer, E.J.; Schultze, J.W. On the influence of microstructure and carbide content of steels on the electrochemical dissolution process in aqueous NaCl electrolytes. *Mater. Corros.* **2002**, *53*, 740–755. [CrossRef]

66. Song, D.; Hao, J.; Yang, F.; Chen, H.; Liang, N.; Wu, Y.; Zhang, J.; Ma, H.; Klu, E.E.; Gao, B.; et al. Corrosion Behavior and Mechanism of Cr–Mo Alloyed Steel: Role of Ferrite/Bainite Duplex Microstructure. *J. Alloys Compd.* **2019**, *809*, 151787. [CrossRef]

67. Zhao, J.; Zhao, X.; Zhao, X.; Dong, C.; Kang, S. Effects of Nucleation Site and Morphology of Carbide-Free Bainite on Microstructures and Properties of Bainite/Martensite Multi-Phase Steels. *Mater. Sci. Eng. A* **2019**, *744*, 86–93. [CrossRef]

68. Qu, S.; Pang, X.; Wang, Y.; Gao, K. Corrosion Behavior of Each Phase in Low Carbon Microalloyed Ferrite–Bainite Dual-Phase Steel: Experiments and Modeling. *Corros. Sci.* **2013**, *75*, 67–77. [CrossRef]

69. Neetu; Katiyar, P.K.; Sangal, S.; Mondal, K. Effect of Various Phase Fraction of Bainite, Intercritical Ferrite, Retained Austenite and Pearlite on the Corrosion Behavior of Multiphase Steels. *Corros. Sci.* **2021**, *178*, 109043. [CrossRef]

70. Xi, Y.; Xie, Z. *Corrosion Effects of Magnesium Chloride and Sodium Chloride on Automobile Components*; Colorado Department of Transportation: Denver, CO, USA, 2002; pp. 1–91.

71. Kristen, D.; Jungert, D.; Gibson, S. *Brine Corrosion Research Study*; Corrpro Canada Inc.: Calgary, AB, Canada, 2019.

72. Lee, C.C.; Mansfeld, F. Analysis of Electrochemical Noise Data for a Passive System in the Frequency Domain. *Corros. Sci.* **1998**, *40*, 959–962. [CrossRef]

73. Xia, D.H.; Song, S.Z.; Behnamian, Y. Detection of Corrosion Degradation Using Electrochemical Noise (EN): Review of Signal Processing Methods for Identifying Corrosion Forms. *Corros. Eng. Sci. Technol.* **2016**, *51*, 527–544. [CrossRef]

74. Xia, D.H.; Qin, Z.; Song, S.; Macdonald, D.; Luo, J.L. Combating Marine Corrosion on Engineered Oxide Surface by Repelling, Blocking and Capturing Cl−: A Mini Review. *Corros. Commun.* **2021**, *2*, 1–7. [CrossRef]

75. Pan, C.; Wang, X.; Behnamian, Y.; Wu, Z.; Qin, Z.; Xia, D.H.; Hu, W. Monododecyl Phosphate Film on LY12 Aluminum Alloy: PH-Controlled Self-Assembly and Corrosion Resistance. *J. Electrochem. Soc.* **2020**, *167*, 161510. [CrossRef]

76. Song, H.J.; Kim, M.K.; Jung, G.C.; Vang, M.S.; Park, Y.J. The Effects of Spark Anodizing Treatment of Pure Titanium Metals and Titanium Alloys on Corrosion Characteristics. *Surf. Coatings Technol.* **2007**, *201*, 8738–8745. [CrossRef]

77. Gaona-Tiburcio, C.; Jáquez-Muñoz, J.M.; Nieves-Mendoza, D.; Maldonado-Bandala, E.; Lara-Banda, M.; Lira-Martinez, M.A.; Reyes-Blas, H.; Baltazar-Zamora, M.Á.; Landa-Ruiz, L.; Lopez-Leon, L.D.; et al. Corrosion Behavior of Titanium Alloys (Ti CP2, Ti-6Al-2Sn-4Zr-2Mo, Ti-6Al-4V and Ti Beta-C) with Anodized and Exposed in NaCl and H$_2$SO$_4$ Solutions. *Metals* **2024**, *14*, 160. [CrossRef]

78. MacDonald, D.D. The History of the Point Defect Model for the Passive State: A Brief Review of Film Growth Aspects. *Electrochim. Acta* **2011**, *56*, 1761–1772. [CrossRef]

79. Macdonald, D.D. The Role of Determinism in the Prediction of Corrosion Damage. *Corros. Mater. Degrad.* **2023**, *4*, 212–273. [CrossRef]

80. Chen, A.; Cao, F.; Liao, X.; Liu, W.; Zheng, L.; Zhang, J.; Cao, C. Study of Pitting Corrosion on Mild Steel during Wet–Dry Cycles by Electrochemical Noise Analysis Based on Chaos Theory. *Corros. Sci.* **2013**, *66*, 183–195. [CrossRef]

81. Lafront, A.M.; Safizadeh, F.; Ghali, E.; Houlachi, G. Study of the Copper Anode Passivation by Electrochemical Noise Analysis Using Spectral and Wavelet Transforms. *Electrochim. Acta* **2010**, *55*, 2505–2512. [CrossRef]

82. Curioni, M.; Skeldon, P.; Koroleva, E.; Thompson, G.E.; Ferguson, J. Role of Tartaric Acid on the Anodizing and Corrosion Behavior of AA 2024 T3 Aluminum Alloy. *J. Electrochem. Soc.* **2009**, *156*, C147. [CrossRef]

83. Ma, Y.; Zhou, X.; Liao, Y.; Chen, X.; Zhang, C.; Wu, H.; Wang, Z.; Huang, W. Effect of Anodizing Parameters on Film Morphology and Corrosion Resistance of AA2099 Aluminum-Lithium Alloy. *J. Electrochem. Soc.* **2016**, *163*, C369–C376. [CrossRef]

84. Li, J.; Du, C.W.; Liu, Z.Y.; Li, X.G.; Liu, M. Effect of Microstructure on the Corrosion Resistance of 2205 Duplex Stainless Steel. Part 2: Electrochemical Noise Analysis of Corrosion Behaviors of Different Microstructures Based on Wavelet Transform. *Constr. Build. Mater.* **2018**, *189*, 1294–1302. [CrossRef]

85. Jáquez-Munõz, J.M.; Gaona-Tiburcio, C.; Cabral, J.A.; Lara-Banda, M.; Estupinãn-López, F.H.; Zambrano, P.; Almeraya-Calderón, F. Corrosion Behavior of Titanium Alloys Using Electrochemical Noise. *ECS Trans.* **2021**, *101*, 167. [CrossRef]

86. Arellano-Pérez, J.H.; Escobar-Jiménez, R.F.; Granados-Lieberman, D.; Gómez-Aguilar, J.F.; Uruchurtu-Chavarín, J.; Alvarado-Martínez, V.M. Electrochemical Noise Signals Evaluation to Classify the Type of Corrosion Using Synchrosqueezing Transform. *J. Electroanal. Chem.* **2019**, *848*, 113249. [CrossRef]

87. Jáquez-Muñoz, J.M.; Gaona-Tiburcio, C.; Cabral-Miramontes, J.; Nieves-Mendoza, D.; Maldonado-Bandala, E.; Olguín-Coca, J.; Estupinán-López, F.; López-León, L.D.; Chacón-Nava, J.; Almeraya-Calderón, F. Frequency Analysis of Transients in Electrochemical Noise of Superalloys Waspaloy and Ultimet. *Metals* **2021**, *11*, 702. [CrossRef]

88. Xia, D.; Mao, Y.; Zhu, Y.; Yuan, Q.; Deng, C.; Hu, W. A novel approach used to study the corrosion susceptibility of metallic materials at a dynamic seawater/air interface. *Corros. Commun.* **2022**, *6*, 62–66. [CrossRef]

89. Ji, Y.; Xu, Y.; Zhang, B.; Behnamian, Y.; Xia, D.; Hu, W. A review of micro-scale and atomic-scale corrosion mechanisms of the second phases in aluminum alloys. *Trans. Nonferrous Met. Soc. China* **2021**, *31*, 3205–3227. [CrossRef]